Radio Science

RESEARCH ARTICLE
10.1029/2018RS006678

A Configuration Space Model for Intermediate-Scale Ionospheric Structure

Charles Rino[1], **Charles Carrano**[1], **Keith Groves**[1], **and Tatsuhiro Yokoyama**[2]

[1]Institute for Scientific Research, Boston College, Chestnut Hill, MA, USA, [2]National Institute of Information and Communications Technology, Tokyo, Japan

Key Points:
- Physics-based structure models connect physical process with abstract structure models
- Striation models can be configured to match in situ and remote diagnostics
- Configuration models provide efficient population of representative data volumes

Correspondence to:
C. Rino,
crino@comcast.net

Citation:
Rino, C., Carrano, C. S., Groves, K. M., & Yokoyama, T. (2018). A configuration space model for intermediate-scale ionospheric structure. *Radio Science*, *53*. https://doi.org/10.1029/2018RS006678

Received 2 JUL 2018
Accepted 26 OCT 2018
Accepted article online 1 NOV 2018

Abstract Stochastic ionospheric structure is characterized by spectral density functions (SDFs), which are formally the average intensity of Fourier transformations of the electron density structure. Structure elongation along magnetic field lines is typically accommodated by constraining contours of constant spatial correlation to field-aligned ellipsoidal surfaces. Structure realizations are generated by imposing the square root of the SDF onto uncorrelated random Fourier modes. The approach has been used successfully for interpreting both in situ and remote propagation diagnostics. However, the only connection to the field-aligned structures generated by the underlying instability mechanism is the correlation scale. This paper introduces a configuration space model that constructs realizations as summations of field-aligned elemental *striations* with a prescribed scale and peak electron density. We show that by choosing the contributing scales according to a bifurcation rule and imposing a power law intensity scaling, the corresponding SDF closely approximates an inverse power law. Thus, configuration space realizations can be structured to reproduce prescribed or measured SDFs from one-dimensional scans. Stochastic variation comes from an imposed random distribution of striation locations, which are defined by their intercept in a reference slice plane. To conform more directly to physics-based simulations, the striations can be interpreted as voids in the background electron density. The model is designed to support propagation simulations with arbitrary propagation angles relative to the local magnetic field direction. Relations between in situ structure and diagnostic measurements as well as phase screen equivalence can be explored.

Plain Language Summary A configuration space ionospheric structure model is described, which generates structure realizations as a summation of physical field-aligned striations. The sized and peak intensity of the striations can be configured to reproduce standard in situ or remote structure diagnostics. The model can be used to overlay structure in global ionospheric models that characterize the background characteristics.

1. Introduction

Global ionospheric models, such as the International Reference Ionosphere (Bilitza & Reinisch, 2015), characterize the background ionosphere and its aggregate motion with deterministic functional representations. Accommodating the stochastic structure generated by unstable configurations requires a statistical characterization of the structure. The most commonly used measure of stochastic ionospheric structure is the spectral density function (SDF), which is formally the average intensity of spatial Fourier decompositions of structure realizations. Because three-dimensional ionospheric structure is highly elongated along the Earth's magnetic field lines, definitive stochastic structure characterization is confined to two-dimensional slice planes penetrated by the field-aligned structure. Conventional ionospheric structure models approximate the anisotropy by constraining spatial coherence to highly elongated elliptical surfaces. Although these models have been used to interpret in situ and propagation diagnostics for decades (Yeh & Liu, 1982), a more direct connection between structural details and the parameters derived from measured SDFs is desirable. This paper develops a configuration space model that provides such a connection.

Recent results from high-resolution physics-based equatorial plasma bubble (EPB) simulations illustrate the structure characteristics. Figure 1, which is taken from Yokoyama (2017), shows a representative EPB structure that resulted from bottomside zonal perturbations applied 1 hr earlier. The structure development is mapped along magnetic field lines that terminate at low altitudes in opposite hemispheres. The left frame shows the

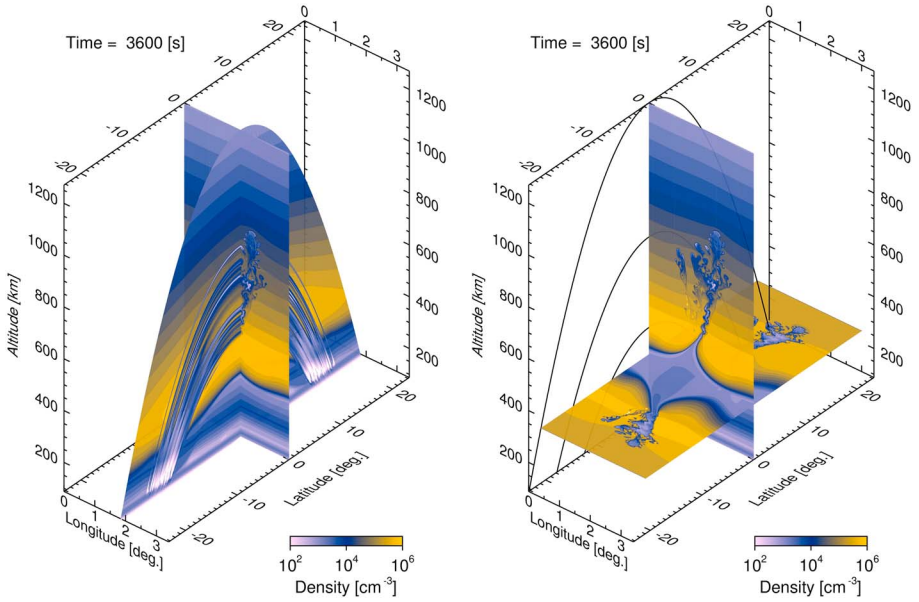

Figure 1. The figure shows a perspective view of the equatorial plasma bubble simulation environment. The left frame highlights the central meridian plane. The right frame shows the structure in horizontal and vertical slice planes.

central meridional slice plane where quasi-deterministic field-aligned structure is manifest. The right frame shows the equatorial cross-field slice plane where the stochastic structure is manifest. The left frame in Figure 2 shows the equatorial plane detail between 300 and 750 km. The right frame shows the cross-field integrated electron density and a smoothed profile (red) that could be compared directly to a global ionospheric model prediction.

High-resolution EPB simulations generate intermediate-scale stochastic structure spanning tens of kilometers to hundreds of meters. At scales approaching tens of kilometers ionospheric structure transitions from

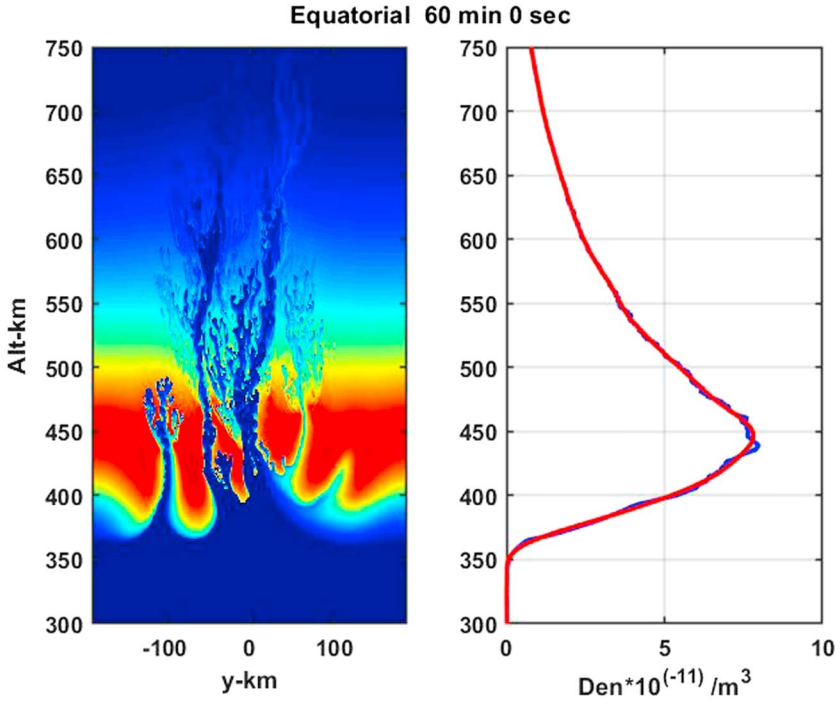

Figure 2. The left frame shows the equatorial plane structure detail. The right frame shows the path-integrated density (blue) with a smoothed profile overlaid (red).

quasi-deterministic to stochastic. Structure smaller than the EPB resolution limit (≈300 m) is governed by spatially dispersive processes. Excluding these contributions from the intermediate-scale range isolates structure that is spatially invariant (frozen) over typical measurement intervals. Ideally, diagnostic measurements are one-dimensional scans of the three-dimensional structure illustrated schematically in Figure 1.

We start with the assumption that the two-dimensional cross-field SDF is isotropic. Analysis of the structure shown in Figure 2 supports the hypothesis. The two-dimensional SDF is denoted $\Phi_{N_e}(q_\perp)$, where $q_\perp$ is the magnitude of the two-dimensional spatial frequency in the equatorial plane. In oblique planes contours of constant electron density are elliptical projections of the assumed cylindrically symmetric structures. The one-dimensional SDF of a diagnostic scan is determined by an integration of the form

$$\varphi_{N_e}(q_y) = \int \Phi_{N_e}(q_\perp)\frac{dq_x}{2\pi}, \tag{1}$$

where $q_\perp = \sqrt{Aq_x^2 + Bq_xq_y + Cq_y^2}$. The coefficients A, B, and C depend on the angle of the magnetic field from the reference axis. The standard modeling approach assigns an integrable analytic form to $\Phi_{N_e}(q_\perp)$. However, configuration space realizations can be constructed by assigning a *target* one-dimensional form to $\varphi_{N_e}(q_y)$ directly. Following the development in Carrano and Rino (2016), the following one-dimensional analytic SDF will be used:

$$\Phi_{N_e}(q) = C_s \begin{cases} q^{-\eta_1} & \text{for } q \le q_0 \\ q_0^{\eta_2-\eta_1} q^{-\eta_2} & \text{for } q > q_0 \end{cases}. \tag{2}$$

In (2), q is the spatial frequency in radians per meter, q_0 is the spatial frequency at which the power law index transitions from η_1 to η_2, and C_s is the turbulent strength. If $\eta_1 = \eta_2$, a single inverse power law applies over the as yet unspecified range of spatial wavenumbers. If $\eta_1 = 0$, the break scale can be interpreted as a conventional outer scale.

A formal relation between (2) and the one-dimensional path-integrated phase SDF is readily established. The orientation of the local coordinate system within which diagnostic measurements are defined is arbitrary, whereby there is no loss of generality in aligning the x axis with the direction of integration. The path-integrated electron density is defined by the integration

$$\phi(y) = \int_L N_e(x,y)dx, \tag{3}$$

where L is the length of the integration path. One can show that the one-dimensional SDF of $\phi(y)$ is

$$\varphi_\phi(q_y) = L^2 \int \frac{\sin^2(q_xL/2)}{(q_xL/2)^2}\Phi_{N_e}(q_x,q_y)\frac{dq_x}{2\pi}. \tag{4}$$

There are two limiting cases

$$\varphi_\phi(q_y) = \begin{cases} L^2\Phi_{N_e}(0,q_y) & \text{for } L >> \sigma \\ L^2\int \Phi_{N_e}(q_x,q_y)\frac{dq_x}{2\pi} & \text{for } L << \sigma \end{cases}, \tag{5}$$

where σ is a measure of the correlation scale along the integration path. Only the first limiting form, which is generally assumed for interpreting propagation diagnostics, provides a direct analytic relation.

We note that the Carrano and Rino (2016) model development assigns the analytic form (2) to the path-integrated phase. The turbulent strength C_s is replaced by C_p, and the spectral indices, η_n, are replaced by p_n. The redefinition of C_s absorbs the radiofrequency-dependent translation of total electron content (TEC) to phase. To the extent that $L >> \sigma$, $p_n = \eta_n + 1$. Correlation along the integration would lead to a path-integrated index closer to the in situ one-dimensional index. The configuration space model can be used to verify the relation between the in situ model parameters and diagnostic measurements.

2. Configuration Space Models

Magnetic field models generate geographic coordinates that trace magnetic field lines. Let $\zeta_s - \zeta_s^k$ represent distance along the kth field line from a reference point ζ_s^k at $\mathbf{r}_k$. Initiation points are placed in a reference slice plane, ideally the equatorial plane. Vector components parallel and normal to the field line in the plane of

curvature, namely, $\zeta_{\parallel}^{k}$ and $\zeta_{\perp}^{k}$, can be constructed at any point along a field line. Curvilinear magnetic field coordinates are defined by the orthogonal vectors ζ_{s}^{k}, $\zeta_{\perp}^{k}$, and $\zeta_{\parallel}^{k} \times \zeta_{\perp}^{k}$. Striation shapes are defined by profile functions, which are monotonically decreasing functions of either distance along the field line, ζ, or radial distance, $|\zeta_{\tau}|$. At the reference point $p_{s}(0) = p_{\perp}(0) = 1$.

The defining equation for a striation is

$$\Delta N_{k}(\zeta_{s}, \zeta_{\tau}) = F_{k} p_{s}(\left|\zeta_{s} - \zeta_{s}^{k}\right| / \sigma_{s}) p_{\perp}(\left|\zeta_{\tau} - \zeta_{\tau}^{k}\right| / \sigma_{k}), \tag{6}$$

where F_k is the striation peak electron density, σ_k is the cross-field scale, and $[\zeta_{s}^{k}, \zeta_{\tau}^{k}]$ identifies the point of initiation. A configuration space realization is constructed by summing the contributions from each striation:

$$\Delta N(\zeta_{s}, \zeta_{\tau}) = \sum_{k=1}^{N_{s}} F_{k} p_{s}(\left|\zeta_{s} - \zeta_{s}^{k}\right| / \sigma_{s}) p_{\perp}(\left|\zeta_{\tau} - \zeta_{\tau}^{k}\right| / \sigma_{k}), \tag{7}$$

where N_s is the number of striations. The initiation points are constrained to lie in a cross-field plane. Extension of each striation along field lines populates a prescribed data space.

2.1. Statistical Characterization

To generate a statistically homogeneous realization, the striation initiation points are drawn from a uniform distribution. With ζ_{τ}^{k} confined to a reference slice plane, (7) simplifies to

$$\Delta N(\zeta_{s}, \zeta_{\tau}) \simeq \sum_{k} F_{k} p_{\perp}(\left|\zeta_{\tau} - \zeta_{\tau}^{k}\right| / \sigma_{k}). \tag{8}$$

The approximation assumes that $p_{s}(\left|\zeta_{s} - \zeta_{s}^{k}\right| / \sigma_{s}) \approx 1$ over the slice plane. Two-dimensional Fourier transforms over oblique slice planes can be computed analytically. Let ρ_s represent the projection of $[\zeta_s, \zeta_\tau]$ onto an oblique slice plane. The two-dimensional Fourier transform of $\Delta N(\rho_s)$ is a summation of the two-dimensional transforms of the projected striation profiles

$$\delta N(\kappa_{s}) \simeq \sum_{k} F_{k} \hat{p}_{\perp}^{(2)}(\kappa_{s}\sigma_{k}) \exp\left\{-i\kappa_{s}\cdot\rho_{s}^{k}\right\}, \tag{9}$$

where

$$\hat{p}_{\perp}^{(2)}(\kappa) = \int p_{\perp}(\eta) \exp\left\{-i\kappa\cdot\eta\right\} \mathrm{d}\eta \tag{10}$$

is the two-dimensional Fourier transform of the projected profile function. If the slice planes are normal to the fields lines, ρ and κ measure position and frequency magnitudes directly. For oblique slice planes, ρ_{s}^{2} and κ_{s}^{2} are quadratic forms representing the projection of the striation cross section and its mapping to the spatial Fourier domain.

The position of each striation imposes a linear phase shift in the spatial Fourier domain. The expectation SDF can be computed as

$$\begin{aligned}\left\langle \left|\Delta N(\kappa_{s})\right|^{2} \right\rangle = {} & \Sigma_{k}\Sigma_{k'} F_{k} \hat{p}_{\perp}^{(2)}(\kappa_{s}\sigma_{k}) F_{k'} \hat{p}_{\perp}^{(2)*}(\kappa_{s}\sigma_{k}) \\ & \times \left\langle \exp\left\{-i(\kappa_{s}\cdot\left(\rho_{\tau}^{k} - \rho_{\tau}^{k'}\right)\right\}\right\rangle.\end{aligned} \tag{11}$$

A uniform distribution of ρ_{τ}^{k} and $\rho_{\tau}^{k'}$ over a sufficiently large area imposes the following formal constraint:

$$\left\langle \exp\left\{-i\kappa_{s}\cdot\left(\rho_{\tau}^{k} - \rho_{\tau}^{k'}\right)\right\}\right\rangle \propto \delta\left(\rho_{\tau}^{k} - \rho_{\tau}^{k'},\right), \tag{12}$$

where $\delta(\cdot)$ is a delta function. Summing the nonzero contributions leads to an analytic representation of the two-dimensional SDF in any slice plane that intercepts field lines

$$\left\langle \left|\Delta N(\kappa_{s})\right|^{2} \right\rangle \propto \sum_{k} F_{k}^{2} \left|\hat{p}_{\perp}^{(2)}(\kappa_{s}\sigma_{k}^{2})\right|^{2}. \tag{13}$$

A similar calculation for a one-dimensional SDF will show that

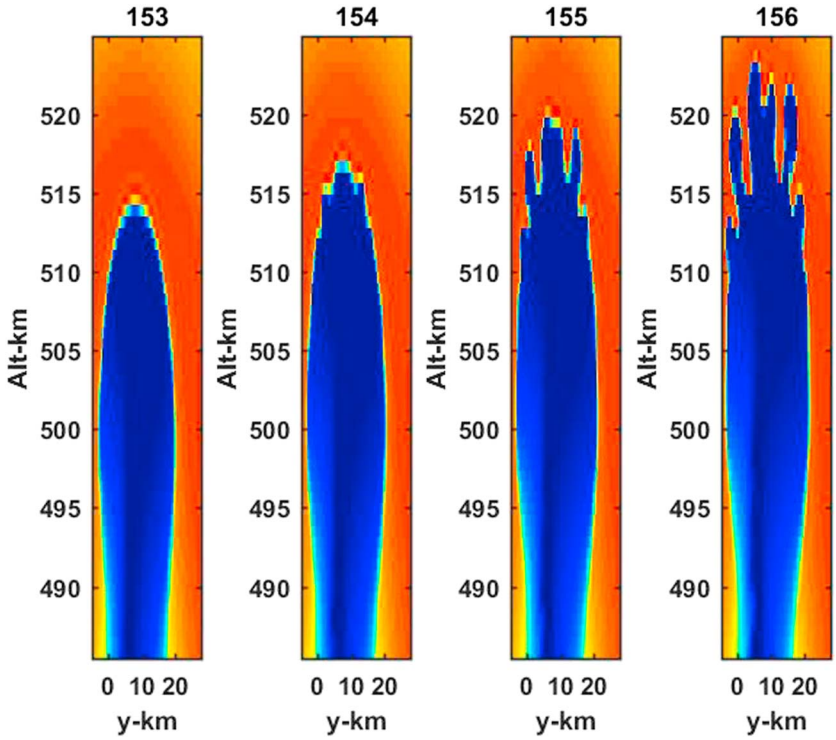

Figure 3. Numbered frames show zoomed views of the central equatorial plasma bubble that generated the structure shown in Figure 2 at 10-s intervals.

$$\left\langle \left|\Delta N(\kappa_s)\right|^2 \right\rangle \propto \sum_k F_k^2 \left|\hat{p}_\perp^{(1)}(\kappa_s \sigma_k^2)\right|^2, \tag{14}$$

where $\hat{p}_\perp^{(1)}(\kappa_s \sigma_k^2)$ is the one-dimensional transform of the radial profile function. These relations apply as long as the striations are distributed uniformly over a sufficiently large data space.

2.2. Successive Bifurcation

To complete the model specification, the number of striations, their peak density, and their scale must be specified. The SDF defines the intensity of each spatial Fourier component. The configuration space parameters F_k and σ_k perform similar defining functions in the spatial domain. The assignment is guided by *successive bifurcation*, which is often invoked to describe the EPB structuring process. Local enhancements with steepening gradients bifurcate by generating local density depletions. The flanking enhancements bifurcate similarly, forming a structure cascade. This is illustrated in Figure 3, which shows four consecutive 10-s zoomed images of the initial development of the central EPB structure in the left frame of Figure 2. A more detailed discussion can be found in Yokoyama et al. (2014).

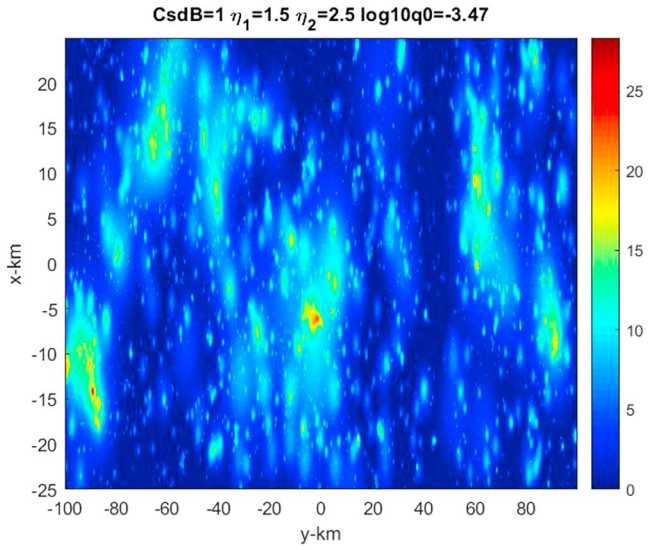

Figure 4. Configuration space realization of two-component power law spectral density function.

Successive bifurcation is captured by the following relations for contributing striation scales, σ_j, and, N_j, the number of striations with scale σ_j

$$\begin{matrix} \sigma_j = \sigma_{\max} 2^{-(J_{\max}-j)} \\ N_j = 2^{d-j} \end{matrix} \quad \text{for } j = 1, 2, \cdots, J_{\max}. \tag{15}$$

The parameter $d \geq J_{\max}$ determines the number of striations at the largest scale, namely, $2^{(d-J_{\max})}$. If $d = J_{\max}$, there is only one striation at the largest scale. Each smaller striation has twice as many striation contributions. The total number of striations is the sum of the number of striations at each scale

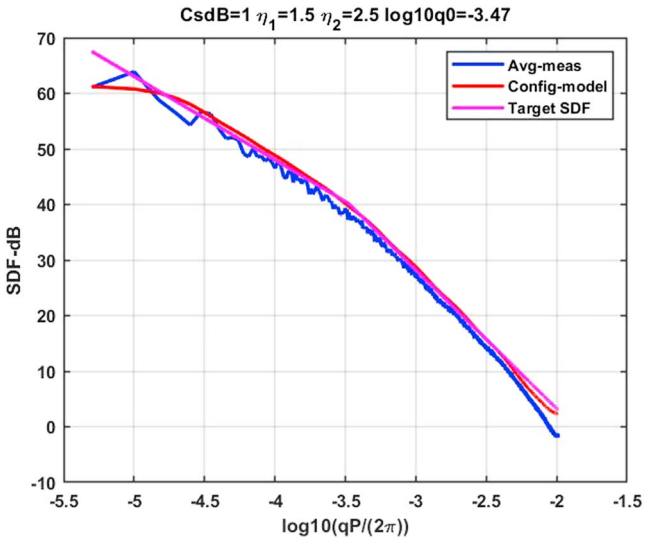

Figure 5. Summary of one-dimensional SDFs for two-component power law realization and average of one-dimensional *y* SDF estimates. SDF = spectral density function.

$$N_s = \sum_j N_j. \tag{16}$$

To complete the configuration space definition, we let

$$F_k = C\sigma_k^{\gamma}, \tag{17}$$

where C and γ are parameters to be determined. We note in passing that the discrete scales represented by σ_j are identical to scales associated with discrete wavelet decompositions (Mallat, 2009).

Substituting (15) and (17) into (14) defines the expectation one-dimensional SDF

$$\left\langle \left|\Delta N(\kappa_s)\right|^2 \right\rangle = C \sum_{k=1}^{N_s} \sigma_k^{2\gamma+1} \left|\hat{p}_{\perp}^{(1)}(\kappa_s)\right|^2. \tag{18}$$

It is understood that σ_k contains the N_j repetitions of σ_j for each contributing scale as defined by (15). Formally, (18) is an analytic expression for the expectation of the one-dimensional SDF of the configuration. From numerical evaluation of (18) we find that the parameter γ and the power law indices are related as

$$\eta = 2\gamma + 2. \tag{19}$$

The parameter C is an overall scale factor that can be chosen so that the variance of each realization is equal in expectation to the integral of the target SDF.

The profile function defines the radial decay of the striation. For computational efficiency the profiles should have finite extent. However, for good SDF definition, the spectral domain sidelobes must decay faster than s^{-2}. We find that the raised cosine

$$p_{\perp}(\rho) = \begin{cases} (1+\cos(2\pi\rho))/2 & \text{for } \rho < 1 \\ 0 & \text{for } \rho \geq 1 \end{cases} \tag{20}$$

provides a good compromise.

2.3. Configuration Space Realization

Generating a configuration space realization starts with a specification of the largest scale, $\sigma_{\max}$, and the number bifurcations, $J_{\max}$, which establish the contributing scale range. An adequate scale range can be checked by comparing an evaluation of (18) with the target SDF (2). The choice of $d > J_{\max}$ determines the total number of striations to be randomly located over the defining plane. Each point in the data space should have contributions from one or more striations. Specifying the remaining parameters, C_s, $\eta_n = (\gamma_n - 1/2)$, and q_0 define the target SDF. Trial and error adjustment of d and $J_{\max}$ can be used to improve the fit to the target SDF.

A two-dimensional realization in the cross-field plane is constructed by using mesh grid coordinates X and Y, which are N_x by N_y matrices that define each point in the data space. In mesh grid coordinates (8) can be written as

$$\Delta N(X,Y) = \sum_{k=1}^{N_s} C(k) p_{\perp}\left(\sqrt{\left(X+\eta_{X_k}\right)^2 + \left(Y+\eta_{Y_k}\right)^2}/\sigma_k\right) \sigma_k^{\gamma(k)}. \tag{21}$$

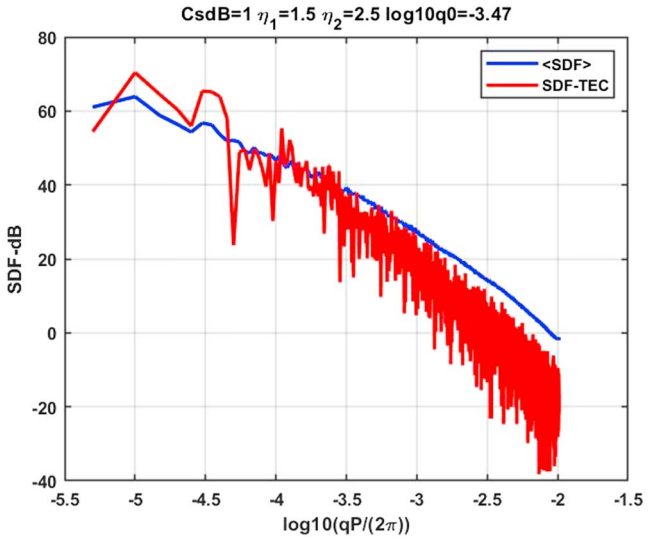

Figure 6. Path-integrated SDF (red) compared to average one-dimensional SDF (blue). SDF = spectral density function.

The variables η_{X_k} and η_{Y_k} are random offsets. As before, it is understood that $C(k)$, $\gamma(k)$, and $\sigma(k)$ capture the bifurcation rules and scaling. Mesh grid sampling and extent determine the spatial wavenumber range, which should capture the spatial frequencies corresponding to the largest and smallest scales.

A representative example with $J_{\max} = 9$, $d = 13$, and $\sigma_{\max} = 50$ km has been constructed. For the defining parameter selection, $N_s = 8,176$ and $\sigma_{\min} = 195.31$ m. A 500 km by 200 km XY mesh grid with $N_x = 2,048$ and $N_y = 4,096$ samples was generated. The cell dimensions are $\Delta x = 24.4$ and $\Delta y = 48.8$. Figure 4 is a color density map of a realization with two-component power law parameters, $C_s = 1$, $\eta_1 = 1.5$, $\eta_2 = 2.5$, and $q_0 = 2\pi/3,000$. Figure 5 verifies the SDF characteristics. The magenta curve is the target SDF as defined by (2). The red curve is the theoretical SDF as defined by (20). The blue curve is the average of 2,048 periodogram estimates derived from realization y scans.

A finer mesgrid sampling will extend the frequency range to reveal the sidelobes of the smallest contributing striations. Similarly, a larger mesh grid will resolve frequencies corresponding to scales larger than $\sigma_{\max}$, where the measured and theoretical SDF achieves a constant value. Statistical equivalence of configuration space realizations implies a common distribution of characteristic scales. The distinctive EPB structure captured in Figure 2 imparts definitive phase relations to the spatial frequencies, which are discarded in the SDF computation.

The extension of (21) to three dimensions is straightforward in regions where the magnetic field lines can be approximated by parallel lines. For an arbitrary rectangular region defined in a topocentric coordinate system, the magnetic field direction can be specified by the unit vector

$$\mathbf{u}_B = -[\cos\theta_B, \sin\theta_B \cos\phi_B, \sin\theta_B \sin\phi_B]. \tag{22}$$

Appendix A.3 in Rino (2011) derives the 3×3 rotation matrix C that transforms a vector in the topocentric system to a magnetic field-aligned system

$$\zeta = C\mathbf{r}. \tag{23}$$

The angle ϕ_B defines the angle of the magnetic meridian plane with respect to the xz plane. The angle θ_B is the angle with respect to the x axis, ~ -90 at the magnetic equator, ~ 0 approaching the magnetic pole. The x axis is the propagation or scan reference direction. Variations along the field lines are ignored, whereby the striations are truncated at the data space boundaries. As already noted, field-aligned curvature and variation can be accommodated.

3. Summary and Conclusions

This paper developed and demonstrated a configuration space model. In its current form the model populates a representative data volume with parallel field lines. Two-component power law SDFs are realized by using a bifurcation rule to populate a defining slice plane such as the equatorial plane shown in Figure 1. The orientation of the magnetic field is arbitrary for a data volume defined by a propagation path or diagnostic probe scan. The current implementation imposes no variation along the direction of the magnetic field. The size distribution in any slice plane perpendicular to the field lines is identical. Structure differences in slice planes normal to the reference axis are manifestations of oblique field line extensions. A cross-field scan generates stochastic variation. Translating propagation paths parallel to the magnetic field also generates stochastic path-integrated structure. However, path ingegration greatly enhances propagation effects. The ramifications for propagation are being pursued and will be reported in subsequent publications.

The Satellite-beacon Ionospheric-scintillation Global Model of the Upper atmosphere model developed by Deshpande et al. (2014) is designed to simulate fully three-dimensional propagation through intermediate-scale structure. Stochastic Satellite-beacon Ionospheric-scintillation Global Model of the Upper

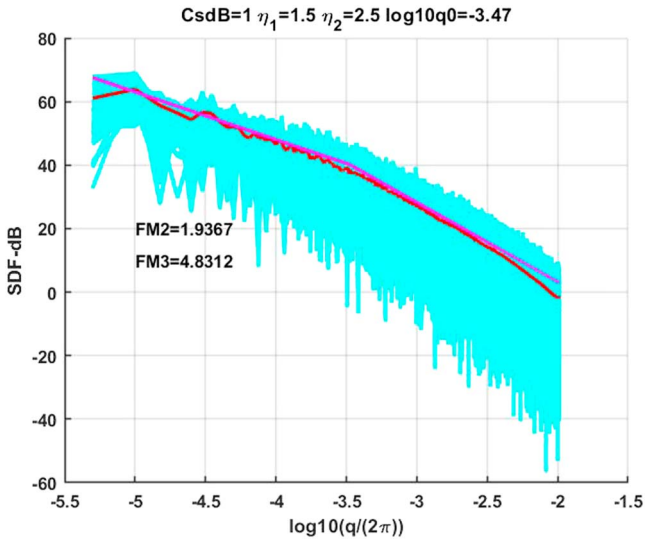

Figure 7. Variation of SDF estimates from configuration space realization. SDF = spectral density function.

atmosphere structure realizations are generated by imposing the amplitude of the desired SDF onto uncorrelated Fourier components. With an appropriately constrained SDF, the realizations are statistically similar to configuration space realizations. However, configurations composed of striations are texturally different, which may have ramifications for interpreting propagation and in situ diagnostics. Three-dimensional Fourier transformations connect every Fourier mode to each point in the data space. In the configuration space model, the contributions to any point in the data space from each striation are independent, whereby parallel processing can be exploited. The realization shown in Figure 4 was executed with 20 min of computation using six processors on a high-end PC.

However, realizations of higher-dimensional intermediate-scale structure are obtained; they provide an opportunity to evaluate diagnostic measurements. In section 1 the connection to propagation diagnostics, which respond to path-integrated structure, was discussed. We showed that the SDF of path-integrated structure depends on the correlation of the structure along the integration path. Figure 6 shows the SDF of the *x* direction path-integrated structure, which is necessarily a single realization (red), overlaid on the average one-dimensional SDF. In the smaller spatial frequency range the path-integrated and average one-dimensional SDFs are similar. In the higher-frequency range the path-integrated one-dimensional SDF falls below the average one-dimensional SDF. The behavior can be understood from (5). The low-frequency range is composed of large-scale structure approaching 50 km, which introduces high correlation over the 50-km integration path. The path-integrated SDF reflects the structure through direct integration. At the higher frequencies, the smaller structure scales are decorrelated along the integration path. In that case the path-integrated SDF is a projection of the two-dimensional structure, which falls off more steeply. Although the relation is more easily understood in terms of configuration space structure, the same behavior would be expected with conventional realizations.

In addition to connecting diagnostic measurement with more robust structure models, configuration space realizations provide a test of a critical assumption for irregularity parameter estimation. The defining parameters are estimated by using a goodness of fit measure applied to periodogram estimates of the one-dimensional SDF. More recent results show that improvements can be realized by using maximum likelihood estimation, which requires prior knowledge of the probability density function of the SDF estimator (Carrano et al., 2017). For realizations generated from linear superpositions of independent Gaussian Fourier components, the statistics of a periodogram estimator is exponential. However, it is known that the periodogram SDF estimate is asymptotically exponential for a broad class of statistically homogeneous processes (Kokoszka & Mikoschb, 2000). Configuration space realizations provide an opportunity to demonstrate the asymptotic exponential relation. Figure 7 shows the variation of the SDF estimates about the nominal mean. The second and third fractional moments

$$F_m = < \hat{\mathrm{SDF}}^m > / < \hat{\mathrm{SDF}} >^m \tag{24}$$

for an exponential distribution $F_2 = 2$ and $F_3 = 6$. The measured moments are shown in the figure. The measured moments are indeed close to the theoretical values for an exponential distribution even though the electron density structure characteristics are very different.

Acknowledgments
The reported research was supported in part by AFRL contract FA9453-12-C-0205, *ADVANCED DATA DRIVEN SPECIFICATION AND FORECAST MODELS FOR THE IONOSPHERE-THERMOSPHERE SYSTEM*. All the results shown in the paper are simulations derived as described in the paper.

References

Bilitza, D., & Reinisch, B. (2015). International reference ionosphere 2007: Improvements and new parameters. *Advances in Space Research*, *42*, 599609.

Carrano, C. S., & Rino, C. L. (2016). A theory of scintillation for two-component power law irregularity spectra: Overview and numerical results. *Radio Science*, *51*, 789813. https://doi.org/10.1002/2015RS005903

Carrano, C. S., Rino, C. L., & Groves, K. M. (2017). Maximum likelihood estimation of phase screen parameters from ionospheric scintillation spectra. In *15th International Ionospheric Effects Symposium* (pp. 1–11) Alexandria, VA, May 9–11.

Deshpande, K. B., Bust, G. S., Clauer, C. R., Rino, C. L., & Carrano, C. S. (2014). Satellite-beacon Ionospheric-scintillation Global Model of the Upper atmosphere (SIGMA) I: High-latitude sensitivity study of the model parameters. *Journal of Geophysical Research: Space Physics*, *119*, 4026–4043. https://doi.org/10.1002/2013JA019699

Kokoszka, P., & Mikoschb, T. (2000). The periodogram at the fourier frequencies. *Stochastic Processes and their Applications*, *86*, 4979.
Mallat, S. (2009). *A wavelet tour of signal processing the sparse way*. Amsterdam: Elsevier Inc.
Rino, C. L. (2011). *The theory of scinillation with applications in remote sensing*. Hoboken, NJ: Wiley.
Yeh, K. C., & Liu, C.-H. (1982). Radio wave scintillations in the ionosphere. *Proceedings of the IEEE*, *70*(4), 324–360.
Yokoyama, T. (2017). A review on the numerical simulation of equatorial plasma bubbles toward scintillation evaluation and forecasting. *Progress in Earth and Planetary Science*, *4*, 37. https://doi.org/10.1186/s40645-017-0153-6
Yokoyama, T. H., Shinagawa, H., & Jin, H. (2014). Nonlinear growth, bifurcation, and pinching of equatorial plasma bubble simulated by three-dimensional high-resolution bubble model. *Journal of Geophysical Research: Space Physics*, *119*, 10,474–10,482. https://doi.org/10.1002/2014JA020708